Journal of Computational Mathematics
Vol.44, No.1, 2026, 232–247.

http://www.global-sci.org/jcm
doi:10.4208/jcm.2410-m2024-0037

NUMERICAL STUDIES OF I-V CHARACTERISTICS IN RESONANT TUNNELING DIODES: A SURVEY OF CONVERGENCE*

Xingming Gao and Haiyan Jiang[1)]
School of Mathematics and Statistics, Beijing Institute of Technology,
Beijing 100081, P.R. China
Emails: xmgao@bit.edu.cn, hyjiang@bit.edu.cn
Tiao Lu
CAPT, LMAM, and School of Mathematical Sciences, Peking University,
Beijing 100871, P.R. China;
Chongqing Research Institute of Big Data, Peking University,
Chongqing 401121, P.R. China
Email: tlu@pku.math.edu.cn
Wenqi Yao
School of Mathematics, South China University of Technology,
Guangzhou 510641, P.R. China
Email: yaowq@scut.edu.cn

Abstract

Resonant tunneling diodes (RTDs) exhibit a distinctive characteristic known as negative resistance. Accurately calculating the tunneling bias energy is indispensable for the design of quantum devices. This paper conducts a thorough investigation into the current-voltage (I-V) characteristics of RTDs utilizing various numerical methods. Through a series of numerical experiments, we verified that the transfer matrix method ensures robust convergence in I-V curves and proficiently determines the tunneling bias for energy potential functions with discontinuities. Our numerical analysis underscores the significant impact of variations in effective mass on I-V curves, emphasizing the need to consider this effect. Furthermore, we observe that increasing the doping concentration results in a reduction in tunneling bias and an enhancement in peak current. Leveraging the unique features of the I-V curve, we employ shallow neural networks to accurately fit the I-V curves, yielding satisfactory results with limited data.

Mathematics subject classification: 65L05, 65Z05, 81Q05, 34C60.
Key words: Schrödinger equation, Transfer matrix methods, Resonant tunneling diodes, Tunneling bias.

1. Introduction

Resonant tunneling diodes are considered to be among the quantum devices with significant potential for practical applications. The RTD is a two-terminal negative resistance nano-device based on the quantum tunneling phenomenon, which has the remarkable advantages of fast response speed, high operating frequency, low voltage, and low power consumption. An RTD consists of a double barrier and a single well connected to an emitter and a collector [11]. RTDs

* Received February 21, 2024 / Revised version received August 7, 2024 / Accepted October 14, 2024 / Published online December 4, 2024 /
1) Corresponding author

are studied in both theory and experiments, and their accurate simulation is very important for developing reliable design tools for quantum devices [20].

Usually, three approaches are used to model quantum transport in RTDs: the wave function [8], the Green function [9, 19], and the Wigner function [13–15]. The Green function method is equivalent to the wave function method for ballistic transport. The Wigner function is defined by the wave function and is very complicated due to the inclusion of the effects of varying effective mass. Thus, the wave function method based on the Schrödinger equation is applied in this paper to study the convergence of I-V curves of RTDs.

The finite difference method (FDM) is a widely used method for the numerical simulation of quantum structures. Employed in solving the Schrödinger equations and the Schrödinger-Poisson system, FDM has demonstrated significant and impactful applications. Cahay and Datta [8] employed FDM to effectively simulate the negative resistance phenomenon in RTDs. Arnold [3,5] introduced a discrete transparent boundary condition based on discrete dispersion relations, extending its utility to the time-dependent Schrödinger equation [2, 4]. Additionally, the finite-difference time-domain method (FDTD) has been successfully utilized in solving the Schrödinger equation in three dimensions, incorporating modified formulas at the incident boundary to achieve numerical solutions through iterative processes [22]. Applications of FDM include its utilization in iteration schemes for the Schrödinger-Poisson system, where FDM has been employed to explore steady-state I-V characteristics [20]. Various iteration techniques have been adopted, including Broyden's method [21], Gummel's iteration with a non-uniform mesh [12], and Newton's iterative method combined with the successive over-relaxation (SOR) method [10].

The transfer matrix method (TMM) has proven to be a versatile tool for investigating bound and scattering states in quantum structures, offering superior accuracy in comparison to FDM [1]. One of the most noteworthy applications of the TMM is to describe the effective solution of the Schrödinger equation with arbitrary potential energy functions, with a specific emphasis on capturing the variation in the effective mass of electrons across different substances during computational processes [17]. Importantly, the numerical accuracy of TMM in solving the Schrödinger equation is substantiated and confirmed in the work presented in [16]. The efficacy of TMM extends comprehensively to a range of applications, including investigations of quantum spin systems [7], fermion models [23], and gamma-rays [6]. TMM was proposed to solve the Schrödinger equation solely, but has never been used in simulation of semiconductor devices.

In the course of our study, we employ TMM, FDM, and the finite volume method (FVM) to solve the Schrödinger equation and the coupled Schrödinger-Poisson system in RTDs. Our investigative results highlight the pronounced convergence of TMM, and notably excelling in accurately capturing tunneling bias energy when compared to the performance of FDM and FVM. Furthermore, our examination delves into the effects stemming from variations in effective mass and doping density on the I-V curves, further contributing to the comprehension and optimization of RTD characteristics. Additionally, we train a neural network with simulation data to predict I-V characteristics across various bias voltages and Fermi energy values, achieving excellent predictive accuracy with a relatively simple network architecture.

This paper is organized as follows. In Section 2, we introduce the structure of 1-D prototype RTDs and the Schrödinger-Poisson system. In Section 3, the numerical methods and the algorithm of the solver for the coupled system are presented. Numerical results are given and explained in Section 4. Finally, our conclusions are given in Section 5.

2. The Schrödinger-Poisson System in RTDs

The 1-D RTD is a typical heterostructure device with negative resistance in certain voltage ranges, which is composed of two thin AlGaAs layers sandwiched between GaAs layers to form two energy barriers and one quantum well, as shown in Fig. 2.1.

The quantum transport model for RTDs is described by the coupled Schrödinger-Poisson system. The Schrödinger equation is

$$-\frac{\hbar^2}{2}\frac{d}{dx}\left(\frac{1}{m(x)}\frac{d}{dx}\psi(x)\right)+V(x)\psi(x)=E\psi(x),\quad x\in(L_0,L_5), \tag{2.1}$$

where $\hbar$ is the reduced Planck constant, $m(x)$ is effective mass, E is energy. $V(x)$ is potential energy function which is related to the external static electric potential energy $U(x)$ by

$$V(x)=U(x)+E_c(x), \tag{2.2}$$

where $E_c(x)$ is the potential energy profile of the conduction band structure for the RTDs which is piecewise constant function as

$$E_c(x)=\begin{cases}0, & L_0\le x\le L_1,\\ E_g, & L_1<x<L_2,\\ 0, & L_2\le x\le L_3,\\ E_g, & L_3<x<L_4,\\ 0, & L_4\le x\le L_5,\end{cases} \tag{2.3}$$

where E_g is the conduction band offset between GaAs and AlGaAs.

From a modeling perspective, we leverage the inherent symmetry of the RTDs to simplify the simulation of double-ended injection. This is achieved by separately modeling it as two reflectionless, single-ended electron injection scenarios, each considered independently at one end. In this model, electrons are injected from one end of the device and are assumed to escape from the opposite end without any reflection, effectively representing the behavior expected in actual device operations. This reflectionless behavior is mathematically represented by applying transparent boundary conditions. Specifically, for electrons injected from the left side, the transparent boundary condition of wave function is modeled as

$$\psi(x)=\begin{cases}\exp(ik_1x)+r\exp(-ik_1x), & x<L_0,\\ t\exp(ik_2x), & x>L_5,\end{cases} \tag{2.4}$$

where $k_1=\sqrt{2m^*E/\hbar^2}>0, k_2=\sqrt{2m^*(E-V_L)/\hbar^2}>0$ or $\mathrm{Im}(k_2)>0$, r is reflection amplitude ($R=|r|^2$ is reflection coefficient), t is the transmission amplitude ($T=|t|^2=1-R$ is transmission coefficient) [13].

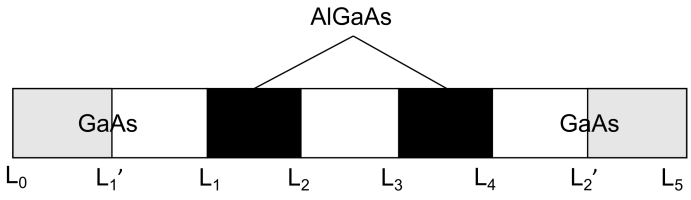

Fig. 2.1. The structure of a typical resonant tunneling diode.

Similarly, for waves injected from the right side, the transparent boundary condition has the form of

$$\psi(x) = \begin{cases} \exp(-ik_2x) + r\exp(ik_2x), & x > L_5, \\ t\exp(-ik_1x), & x < L_0, \end{cases} \tag{2.5}$$

where $k_2 = \sqrt{2m^*(E - V_L)/\hbar^2} > 0$ and $k_1 = \sqrt{2m^*E/\hbar^2} > 0$ or $\mathrm{Im}(k_1) > 0$.

The external static electric potential energy $U(x)$ in (2.2) can be described by the Poisson equation with the Dirichelet boundary condition, which reads

$$\begin{cases} \dfrac{d}{dx}\left(\varepsilon(x)\dfrac{d}{dx}U(x)\right) = q^2\big(N_D(x) - n(x)\big), & x \in (L_0, L_5), \\ U(L_0) = 0, \quad U(L_5) = V_L, \end{cases} \tag{2.6}$$

where $\varepsilon(x)$ is relative dielectric constant, q is charge of an electron, $N_D(x)$ is the donor doping concentration, $n(x)$ is electron density which is related to the distribution of wave functions $\psi_k(x)$ over all possible wave vectors k through

$$n(x) = \frac{mK_BT}{2\pi^2\hbar^2}\int_{-\infty}^{\infty} \ln\left(1 + \exp\left(\frac{\mu - E(k)}{K_BT}\right)\right)|\psi_k(x)|^2\,dk, \tag{2.7}$$

where K_B is the Boltzmann constant, T is the absolute temperature, μ is the Fermi energy, and ψ_k is the wave function corresponding to the wave vector k. For simplification, the function

$$F\big(\mu, E(k)\big) = \ln\left(1 + \exp\left(\frac{\mu - E(k)}{K_BT}\right)\right)$$

is introduced, where $E(k) = \hbar^2k^2/(2m)$ represents the kinetic energy of the electron.

By the dispersion relation $E(k) = \hbar^2k^2/(2m)$, the density can be converted into the integral in kinetic energy space, which reads

$$n(x) = \frac{\sqrt{2m^3}K_BT}{4\pi^2\hbar^3}\int_0^{\infty} \frac{1}{\sqrt{E}}F(\mu, E)\left(\left|\psi_E^l(x)\right|^2 + \left|\psi_{V_L+E}^r(x)\right|^2\right)dE, \tag{2.8}$$

where ψ_E^l is the wave function which satisfies the Schrödinger equation (2.1) with the transparent boundary condition (2.4) when the unit plane wave is injected from the left with energy E, $\psi_{V_L+E}^r$ is the wave function which satisfies the Schrödinger equation (2.1) with the transparent boundary condition (2.5) when the unit plane wave is injected from the right with energy $V_L + E$.

Similarly, according to the Landauer-Buttiker formula, the total current is

$$I(V_L) = \frac{mqK_BT}{2\pi^2\hbar^3}\int_0^{\infty} T(E)\bigg(\ln\left(1 + \exp\left(\frac{\mu - E}{K_BT}\right)\right) - \ln\left(1 + \exp\left(\frac{\mu - E + V_L}{K_BT}\right)\right)\bigg)dE, \tag{2.9}$$

where $T(E)$ is the transmission coefficient corresponding to energy E.

3. Numerical Methods

3.1. Transfer matrix method for the Schrödinger equation

Assuming that a free electron is injected with energy E from the left end of the device at zero bias (equilibrium state), we can solve the wave function $\psi(x)$ for the equilibrium state

analytically as following:

$$\psi(x) = \begin{cases} \exp(\mathrm{i}k_1 x) + r\exp(-\mathrm{i}k_1 x), & L_0 < x < L_1, \\ b_1\exp(\mathrm{i}k_2 x) + b_2\exp(-\mathrm{i}k_2 x), & L_1 \le x \le L_2, \\ b_3\exp(\mathrm{i}k_1 x) + b_4\exp(-\mathrm{i}k_1 x), & L_2 < x < L_3, \\ b_5\exp(\mathrm{i}k_2 x) + b_6\exp(-\mathrm{i}k_2 x), & L_3 \le x \le L_4, \\ t\exp(\mathrm{i}k_1 x), & L_4 < x < L_5, \end{cases} \tag{3.1}$$

where $k_1 = \sqrt{2mE/\hbar^2}$, $k_2 = \sqrt{2m(E-E_g)/\hbar^2}$. Reflection amplitude r, transmission amplitude t and coefficients $b_i,\ i = 1, 2, \ldots, 6$, can be obtained by solving an 8×8 complex linear system according to the continuity of the wave function and flux at L_1, L_2, L_3 and L_4, which can be expressed as

$$\psi(L_i^-) = \psi(L_i^+), \quad \frac{1}{m(L_i^-)}\frac{d\psi(L_i^-)}{dx} = \frac{1}{m(L_i^+)}\frac{d\psi(L_i^+)}{dx}, \quad i = 1, 2, 3, 4.$$

In fact, we can rewrite the linear system as the form of the transfer matrix

$$\begin{pmatrix} 1 \\ r \end{pmatrix} = M_1 \begin{pmatrix} b_1 \\ b_2 \end{pmatrix}, \quad \begin{pmatrix} b_1 \\ b_2 \end{pmatrix} = M_2 \begin{pmatrix} b_3 \\ b_4 \end{pmatrix}, \quad \begin{pmatrix} b_3 \\ b_4 \end{pmatrix} = M_3 \begin{pmatrix} b_5 \\ b_6 \end{pmatrix}, \quad \begin{pmatrix} b_5 \\ b_6 \end{pmatrix} = M_4 \begin{pmatrix} t \\ 0 \end{pmatrix}, \tag{3.2}$$

thus r and t are determined by

$$\begin{pmatrix} 1 \\ r \end{pmatrix} = M \begin{pmatrix} t \\ 0 \end{pmatrix}, \tag{3.3}$$

where $M = M_1 M_2 M_3 M_4$ is the transfer matrix. Obviously,

$$t = \frac{1}{M(1,1)}, \quad r = \frac{M(2,1)}{M(1,1)},$$

where $M(i, j)$ is the element corresponding to the i-th row and j-th column of the matrix M. Once the matrix M is calculated, the transmission coefficient and the wave function can be attained analytically. This is the transfer matrix method. From this simple case, we can know that for piecewise constant potential function, TMM gives the correct solution.

Actually, the TMM can be applied to Schrödinger equations with arbitrary potential. The domain of the device is divided uniformly by the step size $\Delta x = \overline{L_0 L_5}/N$, and the knots $x_j = j\Delta x,\ j = 0, \ldots, N$, include the boundary of AlGaAs and GaAs. The potential function is approximated by piecewise constant function

$$V(x) = \sum_{j=0}^{N-1} V_j I_{(x_j, x_{j+1})},$$

where $I_{(x_j, x_{j+1})}$ is the indicator function of (x_j, x_{j+1}), constant $V_j = (V(x_j^+) + V(x_{j+1}^-))/2$, $V(x_j^+)$ is the right limit of V at x_j, and $V(x_{j+1}^-)$ is the left limit of V at x_{j+1}. The wave function in (x_j, x_{j+1}) is approximated by

$$\psi(x) = A_j \exp(ik_j x) + B_j \exp(-ik_j x),$$

where $k_j = \sqrt{2m(E - V_j)/\hbar^2}, A_0 = 1, B_0 = r, A_N = t, B_N = 0$. Similarly, by the continuity of the wave function and flux at interior knots, r and t are unknown constants and can be calculated through

$$\begin{pmatrix} 1 \\ r \end{pmatrix} = M \begin{pmatrix} t \\ 0 \end{pmatrix}, \tag{3.4}$$

where $M = M_1 M_2 \cdots M_N$. TMM only needs to calculate 2×2 matrix multiplication and inversion, thus it can be implemented very efficiently.

3.2. FVM and FDM for Schrödinger equation

Integrating the Schrödinger equation (2.1) on the subinterval $[x_{j-1/2}, x_{j+1/2}]$ and then applying the central difference $d\psi/dx|_{x_{j+1/2}} \approx (\psi_{j+1} - \psi_j)/\Delta x$, a finite volume discretization of the Schrödinger equation can be expressed as

$$-\frac{\hbar^2}{2m_{j+1/2}}\frac{\psi_{j+1}-\psi_j}{\Delta x^2} + \frac{\hbar^2}{2m_{j-1/2}}\frac{\psi_j-\psi_{j-1}}{\Delta x^2} + \left(\frac{V(x_j^+)+V(x_j^-)}{2} - E\right)\psi_j = 0, \tag{3.5}$$

where ψ_j is approximate value of $\psi(x_j)$ and $m_{j+1/2} = m(x_{j+1/2})$ is the effective mass at $x_{j+1/2}$.

If the center difference method is used directly, a finite difference scheme for the Schrödinger equation (2.1) is given

$$-\frac{\hbar^2}{2m_{j+1/2}}\frac{\psi_{j+1}-\psi_j}{\Delta x^2} + \frac{\hbar^2}{2m_{j-1/2}}\frac{\psi_j-\psi_{j-1}}{\Delta x^2} + \big(\bar{V}(x_j) - E\big)\psi_j = 0, \tag{3.6}$$

where $\bar{V}(x_j) = \min(V(x_j^+), V(x_j^-))$ is the smaller one-side limit of V at x_j, and $j = 0, 1, 2, \ldots, N$.

Although (3.5) and (3.6) are different only in the last term, it is verified numerically that there are big differences in simulating the I-V curves for RTDs, the reason is that two methods approximate the square barrier differently. The discontinuity of potential function is ignored in FDM, while it is linearized in FVM. Eqs. (3.5) and (3.6) are equipped with the discrete transparent boundary conditions, which are discretized exactly as

$$\begin{cases} \psi_{-1} = \exp(-ik_1\Delta x) + (\psi_0 - 1)\exp(ik_1\Delta x), \\ \psi_{N+1} = \exp(ik_2\Delta x)\psi_N \end{cases} \tag{3.7}$$

for the wave injected from the left, and

$$\begin{cases} \psi_{-1} = \psi_0 \exp(ik_1\Delta x), \\ \psi_{N+1} = \exp(ik_2\Delta x)\psi_N + \exp(-ik_2 L)\big(-2i\sin(k_2\Delta x)\big) \end{cases} \tag{3.8}$$

for the wave injected from the right.

3.3. Iteration method for the Schrödinger-Poisson system

The finite difference approximation of the Poisson equation (2.6) is given by

$$\frac{\varepsilon_{j-1/2}}{\Delta x^2}U_{j-1} - \frac{\varepsilon_{j-1/2}+\varepsilon_{j+1/2}}{\Delta x^2}U_j + \frac{\varepsilon_{j+1/2}}{\Delta x^2}U_{j+1} - q^2\big(N_D(x_j) - n_j\big) = 0, \tag{3.9}$$

where $\varepsilon_{j+1/2}$ represents the dielectric constant at the midpoint between grid points, U_j is approximate value of $U(x_j)$, and $N_D(x_j)$ corresponds to the doping concentration at x_j.

Due to nonlinearity of the Schrödinger-Poisson system, we can rewrite (3.9) as matrix form

$$F(\hat{U}) \triangleq A\hat{U} - q^2\big(\hat{N}_D - \bar{n}(x, \hat{U})\big) + W = 0, \tag{3.10}$$

where $\hat{U}, W, \hat{N}_D, \bar{n}(x,\hat{U})$ are vectors, which read

$$\begin{aligned}
&\hat{U} = [U_1, U_2, \cdots, U_{N-1}]^\top, \\
&W = \left[\frac{\varepsilon_{1/2}}{\Delta x^2}U(0), 0, \cdots, 0, \frac{\varepsilon_{N-1/2}}{\Delta x^2}U(L)\right]^\top, \\
&\hat{N}_D = [N_D(x_1), N_D(x_2), \cdots, N_D(x_{N-1})]^\top, \\
&\bar{n}(x,\hat{U}) = [n(x_1,\hat{U}), \cdots, n(x_{N-1},\hat{U})]^\top,
\end{aligned} \tag{3.11}$$

and A is a symmetric tri-diagonal matrix, given by

$$A = \begin{bmatrix}
-\frac{\varepsilon_{1/2}+\varepsilon_{3/2}}{\Delta x^2} & \frac{\varepsilon_{3/2}}{\Delta x^2} & & & \\
\ddots & \ddots & & & \\
\frac{\varepsilon_{j-1/2}}{\Delta x^2} & -\frac{\varepsilon_{j-1/2}+\varepsilon_{j+1/2}}{\Delta x^2} & \frac{\varepsilon_{j+1/2}}{\Delta x^2} & & \\
 & \ddots & \ddots & & \\
 & & \frac{\varepsilon_{J-3/2}}{\Delta x^2} & -\frac{\varepsilon_{J-3/2}+\varepsilon_{J-1/2}}{\Delta x^2}
\end{bmatrix}. \tag{3.12}$$

In order to improve the accuracy of the solution to (3.10), it is assumed that the density function $n(x)$ is related to the potential function $U(x)$ like the Maxwell-Boltzmann distribution, that is $n(x,U) \propto \exp(-U/(K_B T))$ [10]. As a result, the Jacobian of F with respect to $\hat{U}$ is approximated by

$$J = A - \mathrm{diag}\left\{q^2 \frac{1}{K_B T}\bar{n}(x,\hat{U})\right\}. \tag{3.13}$$

With the initial guess $U^{(0)}$, the Newton-Raphson iteration scheme is

$$\hat{U}^{(n+1)} = \hat{U}^{(n)} - J^{-1}F(\hat{U}^{(n)}). \tag{3.14}$$

We summarize the algorithm for simulating I-V characteristics of RTDs in Algorithm 3.1.

Algorithm 3.1: Algorithm for the I-V Characteristics of RTD.

Given an error tolerance $tol > 0$ and the external bias potential energy V_L.

1. Guess initial potential energy $U^{(0)}$.
2. $V = U^{(0)} + E_c(x)$.
3. Solve the Schrödinger equation (2.1) with the TMM (FVM, or FDM) and integrate in energy space to calculate electron density $n(x)$ according to (2.8).
4. Substitute the density function $n(x)$ into the Poisson equation (2.6) and apply the Newton-Raphson iteration (3.14) to calculate the external static electric potential energy $U^{(1)}$.
5. If $\|U^{(0)} - U^{(1)}\|_\infty < tol$, then $U^{(1)}$ is the convergent potential energy. Otherwise, set $U^{(0)} = U^{(1)}$, and repeat steps 2-5.
6. Calculate the transmission coefficient $T(E)$ by solving the Schrödinger equation (2.1) with the TMM (FVM, or FDM) using the convergent external potential $U^{(1)}$ and $V = U^{(1)} + E_c(x)$. Integrate in energy space and obtain the total current $I(V_L)$ according to (2.9).

4. Numerical Results

The RTD exhibits negative differential resistance (NDR) characteristics, which positions it as a promising candidate for applications in high-frequency oscillators, logic circuits, and memory devices. The precise determination of I-V curves is crucial for establishing the tunneling bias, which plays an important role in designing the device. TMM, FVM, and FDM are employed to investigate the convergence of I-V curves in RTDs which have symmetrical structure as Fig. 2.1.

4.1. Convergence of I-V characteristics

In order to investigate the convergence of Algorithm 3.1, we adopted a specific RTD, which is the same with that is studied in [12, 20]. Parameters of the device are set as follows: the overall length $\overline{L_0L_5} = 135$ nm, the lengths of the barriers $\overline{L_1L_2} = \overline{L_3L_4} = 5$ nm, and the length of the well $\overline{L_2L_3} = 5$ nm. For the sake of computational simplicity, we make the assumption that $L_0 = 0$. The Fermi energy is set to $\mu = 0.067097$ eV, the effective mass for electrons in both GaAs and AlGaAs are unified as $m_{\text{GaAs}} = m_{\text{AlGaAs}} = 0.067m_e$, and the relative dielectric constants of GaAs and AlGaAs are unified as $\varepsilon_{\text{GaAs}} = \varepsilon_{\text{AlGaAs}} = 11.4\varepsilon_0$. The else constants used in numerical simulation are listed as $\hbar = 1.05467 \times 10^{-34}$ J.s, $K_B = 1.38065 \times 10^{-23}$ J/K, $T = 300$ K, $\varepsilon_0 = 8.845 \times 10^{-12}$ F/m, $m_e = 9.10938 \times 10^{-31}$ kg, $E_g = 0.3$ eV, and the doping concentration is

$$N_D(x) = \begin{cases} 10^{-3}/\text{nm}^{-3}, & L_0 \le x \le L_1^{'}, \\ 10^{-3}/\text{nm}^{-3}, & L_2^{'} \le x \le L_5, \\ 10^{-6}/\text{nm}^{-3}, & \text{otherwise}, \end{cases}$$

where $L_1^{'} = 50$ nm and $L_2^{'} = 85$ nm.

4.1.1. Fixed potential

Firstly, a fixed potential energy $V(x) = U(x) + E_c(x)$ is considered, where

$$U(x) = \begin{cases} 0, & L_0 \le x < L_1^{'}, \\ \dfrac{x - L_1^{'}}{L_2^{'} - L_1^{'}} V_L, & L_1^{'} \le x \le L_2^{'}, \\ V_L, & L_2^{'} < x \le L_5. \end{cases} \tag{4.1}$$

It is noteworthy that normally $E_c(x)$ is a piecewise constant function. Before we investigate the convergence of I-V curves for the discontinuous potential energy function, the convergence for a smooth potential distribution $E_{cs}(x)$ is studied. $E_{cs}(x)$ is the smoothed version of $E_c(x)$ via convolution with a kernel function $\phi(x) = 5\exp(5x)/(1 + \exp(5x))^2$, thus it can be expressed as

$$\begin{aligned} E_{cs}(x) &= \int_0^{L_5} E_c(y)\phi(x - y)dy \\ &= \frac{E_g}{1 + \exp\big(5(x - L_2)\big)} - \frac{E_g}{1 + \exp\big(5(x - L_1)\big)} \\ &\quad + \frac{E_g}{1 + \exp\big(5(x - L_4)\big)} - \frac{E_g}{1 + \exp\big(5(x - L_3)\big)}, \end{aligned} \tag{4.2}$$

which is depicted in Fig. 4.1.

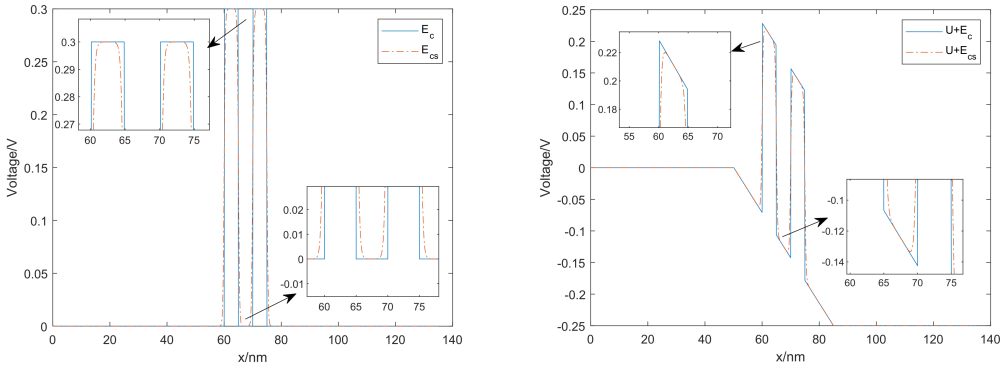

(a) E_c and E_{cs} (b) The smooth flatband potential with $V_L = -0.25$ eV

Fig. 4.1. The smooth flatband potential.

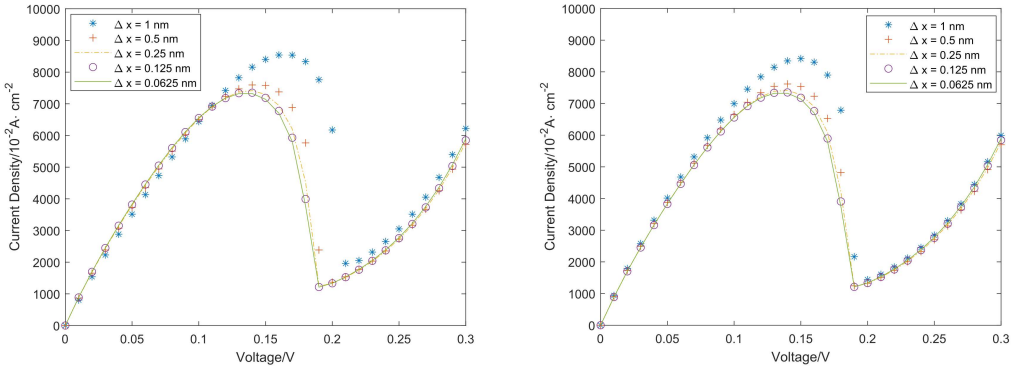

(a) The I-V curves generated by the TMM (b) The I-V curves generated by the FVM (FDM)

Fig. 4.2. The convergence of I-V curves with the smooth potential ($E_{cs} + U$).

For a continuous potential energy function, the FVM and the FDM employed in this study are equivalent for solving the Schrödinger equation. Numerical results illustrated in Fig. 4.2 demonstrate that the TMM and the FVM (FDM) both exhibit preferably convergence for the I-V curves generated by solving the Schrödinger equation with the smooth flatband potential $U + E_{cs}$.

The presence of discontinuity in $E_c(x)$ arises from distinct components of the device. The discontinuity should be precisely included for practical devices. Fig. 4.3 elucidates the convergence of the I-V curves through numerically solving the Schrödinger equation with the flatband potential $U + E_c$. Notably, the comparison under the context of the discontinuous potential reveals the superior convergence of I-V curves achieved by the TMM, in contrast to those achieved by the FVM and the FDM. However, the I-V curves generated by the three methods converge to the same curve, thus verifying the reliability of the three methods.

4.1.2. Self-consistent potential

Secondly, the external potential energy $U(x)$ is obtained by solving the (2.6) self-consistently with (2.1), according to Algorithm 3.1. The I-V curves illustrated in Fig. 4.4 reveal that the TMM has better overall convergence behavior compared to the FVM and the FDM. Fig. 4.4(d) shows the I-V curves obtained by the TMM with the finest mesh size of $\Delta x = 0.0625$ nm, the

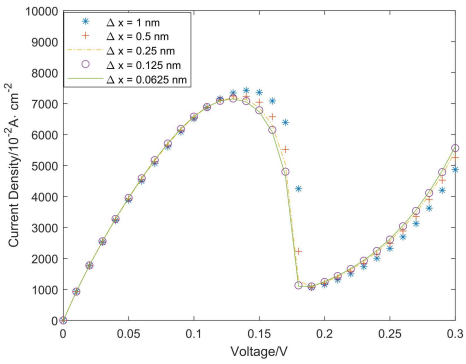

(a) The I-V curves generated by TMM

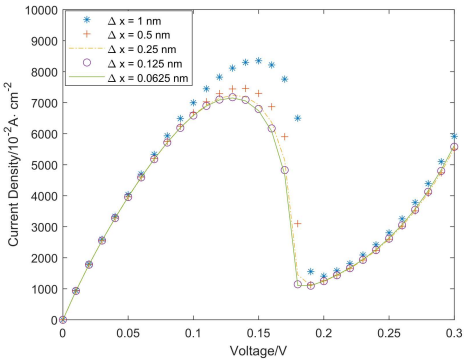

(b) The I-V curves generated by FVM

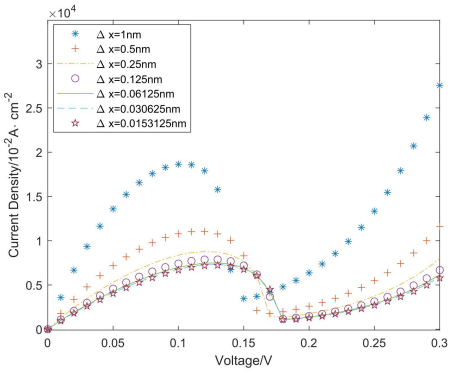

(c) The I-V curves generated by FDM

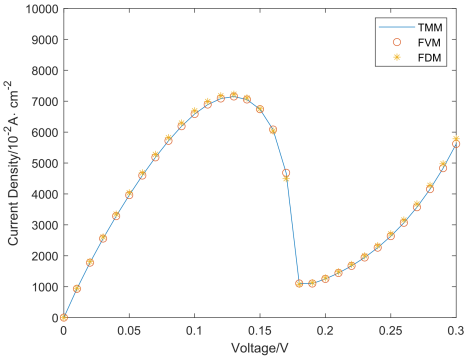

(d) The numerically convergent I-V curves

Fig. 4.3. The convergence of I-V curves simulated with the discontinuous potential $(E_c + U)$ by using the three methods, respectively.

FVM with $\Delta x = 0.0625$ nm, and the FDM with $\Delta x = 0.0153125$ nm. It is evident that the TMM and the FVM yield results that are more consistent with each other. Nevertheless, it is noteworthy that the I-V curve computed by the TMM has already achieved convergence at the mesh size of $\Delta x = 1$ nm, while the FVM necessitates the mesh size $\Delta x = 0.25$ nm for the convergence result, and the FDM requires $\Delta x = 0.06125$ nm. This observation implies that the TMM stands out as a more efficient method for the coupled system.

The convergence of I-V curves is closely related to the convergence of both the electron density $n(x)$, and the potential function $U(x)$. When the potential $U(x) \equiv 0$ is applied to solve the Schrödinger equation through the TMM, the FVM, and the FDM, the convergence behavior of the electron densities corresponding to the three methods is depicted in Fig. 4.5. A detailed comparison among Figs. 4.5(a)-4.5(c) indicates that the electron densities solved by the TMM converge much more rapidly in contrast to that solved with either the FVM or the FDM. Figs. 4.5(d)-4.5(f) respectively illustrate the convergence of the potential energy function calculated by the TMM, the FVM, and the FDM, where faster convergence is observed in solutions solved with the TMM than that solved with either the FVM and the FDM.

The numerical result, for the I-V curves, the electron densities $n(x)$, and the potential energy $U(x)$ consistently demonstrate the robust convergence of the TMM, while the FDM exhibits the least favorable convergence. Despite the FDM being capable of calculating the negative resistance effect, the I-V curves obtained with the FDM deviate significantly from the accurate results achieved through the TMM and the FVM, which could be told from Fig. 4.4(d).

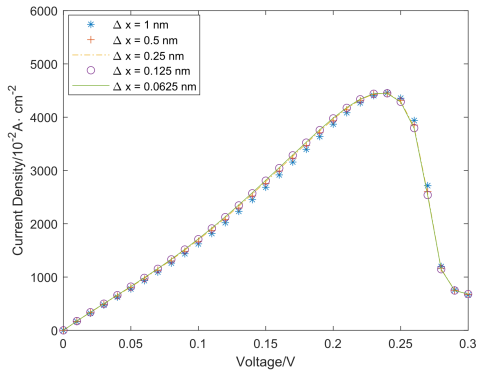

(a) The I-V curves generated by the TMM

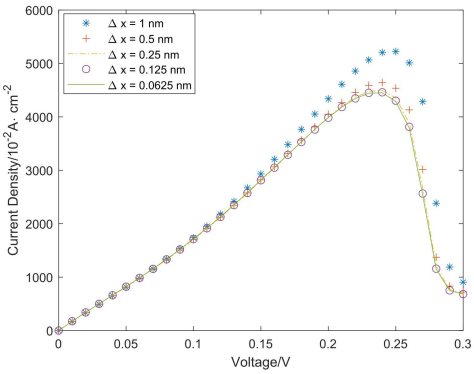

(b) The I-V curves generated by the FVM

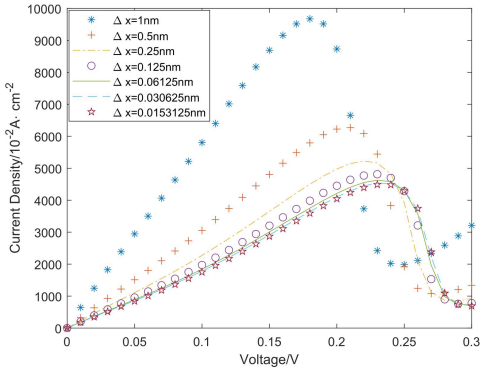

(c) The I-V curves generated by the FDM

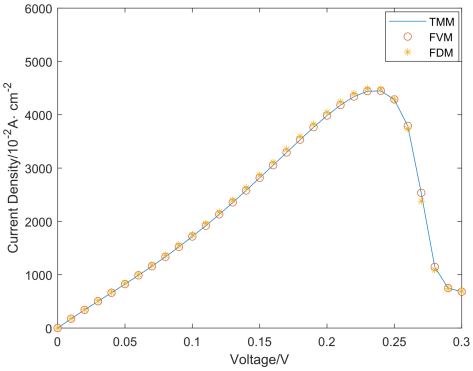

(d) The numerically convergent I-V curves

Fig. 4.4. The convergence of I-V curves generated by the coupled system using the three methods, respectively.

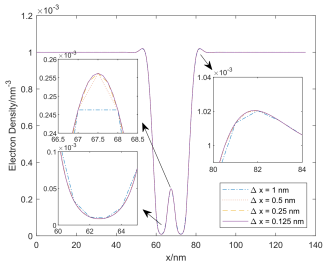

(a) The electron density generated by the TMM with $U(x) \equiv 0$

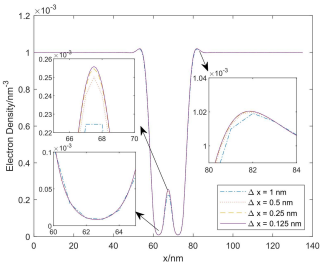

(b) The electron density generated by the FVM with $U(x) \equiv 0$

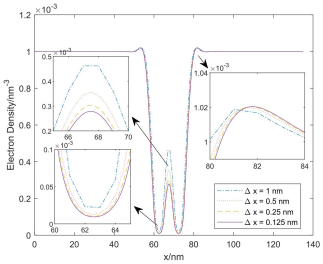

(c) The electron density generated by the FDM with $U(x) \equiv 0$

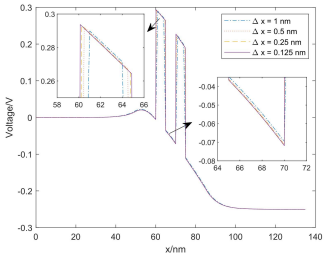

(d) The potential energy generated by the TMM with $V_L = -0.25$ eV

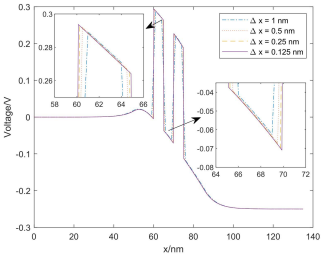

(e) The potential energy generated by the FVM with $V_L = -0.25$ eV

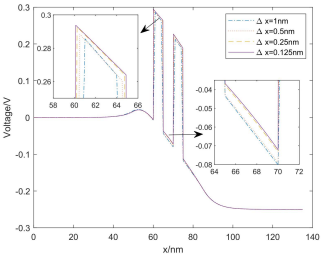

(f) The potential energy generated by the FDM with $V_L = -0.25$ eV

Fig. 4.5. The convergence of the electron density and the potential energy simulated by using the three methods, respectively.

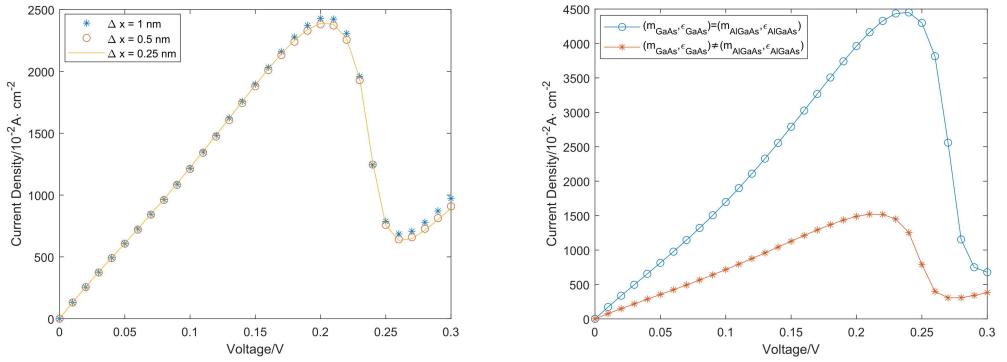

(a) The convergence of I-V curves with the specified parameters

(b) The I-V curves for the uniform parameters and specified parameters

Fig. 4.6. The I-V curves derived from the TMM with various parameter combinations of effective mass and relative dielectric constant.

This discrepancy can be attributed to the primary distinction among the TMM, the FVM, and the FDM in their abilities to capture potential energy discontinuity. The FDM employs a direct assignment with one-side limit, while the FVM linearizes the discontinuities in the potential energy function. However, the TMM, by accurately addressing the discontinuities in potential energy, exhibits superior capability in faithfully capturing the complex features of RTDs.

Thirdly, we explore the numerical effects of the varying effective mass and relative dielectric constants of GaAs and AlGaAs on the I-V curves. We subsequently implement the TMM in Algorithm 3.1 with the specified parameters: $m_{\text{AlGaAs}} = 0.0912m_e$, $m_{\text{GaAs}} = 0.067m_e$, $\varepsilon_{\text{AlGaAs}} = 12.03\varepsilon_0$, $\varepsilon_{\text{GaAs}} = 12.9\varepsilon_0$. As depicted in Fig. 4.6(a), the I-V curves obtained through the TMM exhibit highly favorable convergence. Furthermore, Fig. 4.6(b) shows that the I-V curves with varying parameters are significantly different from those with the uniform parameters. This observation underscores that the variance in effective mass and relative dielectric constant of GaAs and AlGaAs cannot be neglected for precise I-V characteristics.

4.2. Effect of doping concentration on the I-V characteristics

Finally, we investigate the influence of the doping concentration on the I-V characteristics of RTDs. RTD devices investigated in this section share following structural parameters: $\overline{L_0L_5} = 81.925$ nm, $\overline{L_1L_2} = \overline{L_3L_4} = 4.52$ nm, $\overline{L_2L_3} = 2.825$ nm, $\overline{L_0L_1'} = \overline{L_2'L_5} = 17.515$ nm. The conduction band offset between GaAs and AlGaAs E_g is set to 0.27 eV. Noting that the quantum tunneling phenomenon is more pronounced at low temperatures, we adjusted the temperature T from room temperature (300 K) to that of liquid nitrogen (77 K).

By employing the Fermi-Dirac integral, the connection between the Fermi energy μ and the doping concentration N_0 within the heavily doped region can be expressed as [18]

$$N_0 = 2\left(\frac{m^* K_B T}{2\pi\hbar^2}\right)^{\frac{3}{2}} F_{\frac{1}{2}}\left(\frac{\mu}{K_B T}\right), \tag{4.3}$$

where $F_{1/2}(x)$ is the Fermi-Dirac integral, which reads

$$F_{\frac{1}{2}}(x) = \frac{2}{\sqrt{\pi}}\int_0^\infty \frac{\sqrt{x}}{1+\exp(x-z)}dx.$$

Hence, the doping concentration function is given by

$$N_D(x) = \begin{cases} N_0, & L_0 \le x \le L_1', \\ N_0, & L_2' \le x \le L, \\ \alpha N_0, & \text{otherwise}, \end{cases}$$

where $\alpha \in [0, 1)$ is the ratio of the doping concentration in the lightly doped region to that in the heavily doped region.

In Fig. 4.7(a), with the ratio α set to zero and an increase in the Fermi energy μ, higher doping concentration N_0 lead to an increase in peak current and a decrease in the first tunneling bias voltage. These observations align with the results from the Wigner equation [24]. However, when maintaining a constant doping concentration N_0 in the heavily doped region, altering the ratio α in the lightly doped region results in a distinct change in the I-V curve. Fig. 4.7(b) illustrates that an increase in the doping concentration in the lightly doped region leads to a decrease in the first tunneling bias voltage, along with a slight increase in peak current. Thus, strategically increasing the doping concentration throughout the entire device holds the potential to reduce tunneling bias and enhance the peak current. It is evident that μ has a significant impact on the I-V curves.

Noticing that the I-V curve exhibits pronounced negative differential resistance effect, it poses a considerable challenge to derive an analytical expression for it. With advancements in neural network technology, more efficient fitting models can be trained even with limited datasets. Recognizing the significance of μ in influencing the I-V curve, we employed a shallow neural network structure with inputs $(\mu, v_b := V_L/q)$ to establish a simplified functional representation. The structure of the N-layer neural network consists of N hidden layers, each with six neurons, as depicted in Fig. 4.8. The activation function is of sigmoid type and the optimization algorithm employed is the Levenberg-Marquardt algorithm. By training neural networks with two to five hidden layers and utilizing I-V curve data, good prediction of I-V curves can be achieved without solving the Schrödinger-Poisson system. The training dataset includes 488 data points for the I-V curves with bias voltage values $v_b = 0 : 0.01 : 0.6$ (V) and the Fermi energy values $\mu = 0.08, 0.10, 0.13, 0.16, 0.20, 0.22, 0.25, 0.318$ (eV).

Next, we applied Algorithm 3.1 to compute the I-V curve at $\mu = 0.28$ eV as a reference and used the trained network to predict the I-V curve at the same μ. The results are shown in Fig. 4.9.

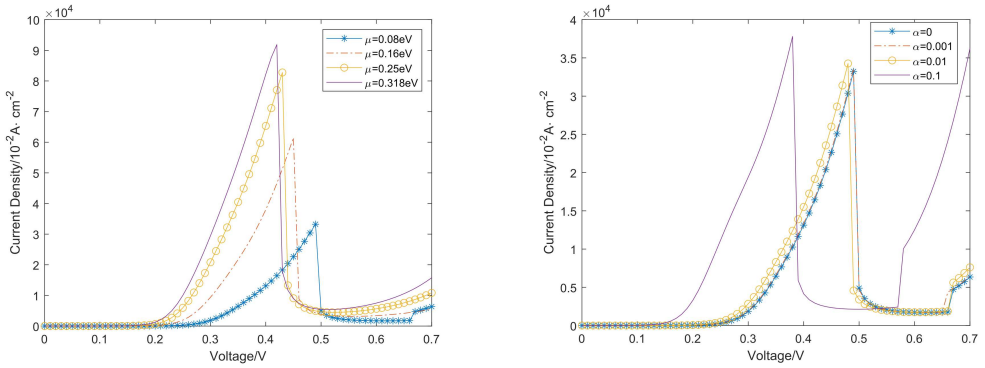

(a) The I-V curves with various μ ($\alpha = 0$)

(b) The I-V curves with various α ($\mu = 0.08$ eV)

Fig. 4.7. The I-V curves obtained by the TMM with various μ and α.

In Fig. 4.9, the trained neural networks demonstrate satisfactory performance in predicting the I-V curve, with those outputs closely matching the reference. Furthermore, an increase in the number of hidden layers has demonstrated an improvement in the predictive performance of the neural networks.

The above results suggest the potential for employing neural networks to develop a comprehensive fitting model that encompasses all structural parameters of RTDs with abundant I-V curve data.

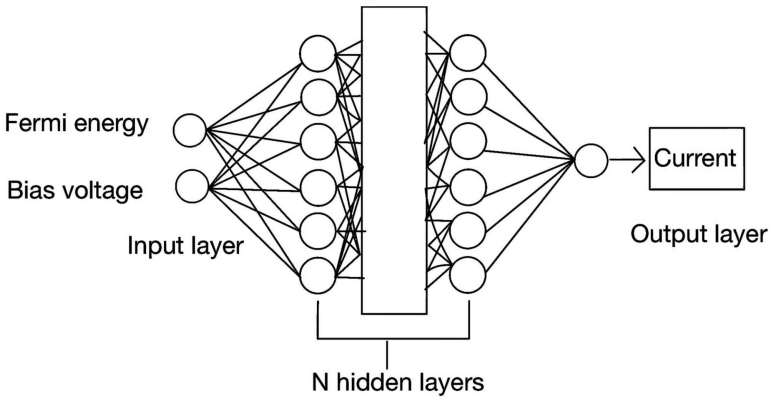

Fig. 4.8. The structure of N hidden layers fully connected neural network.

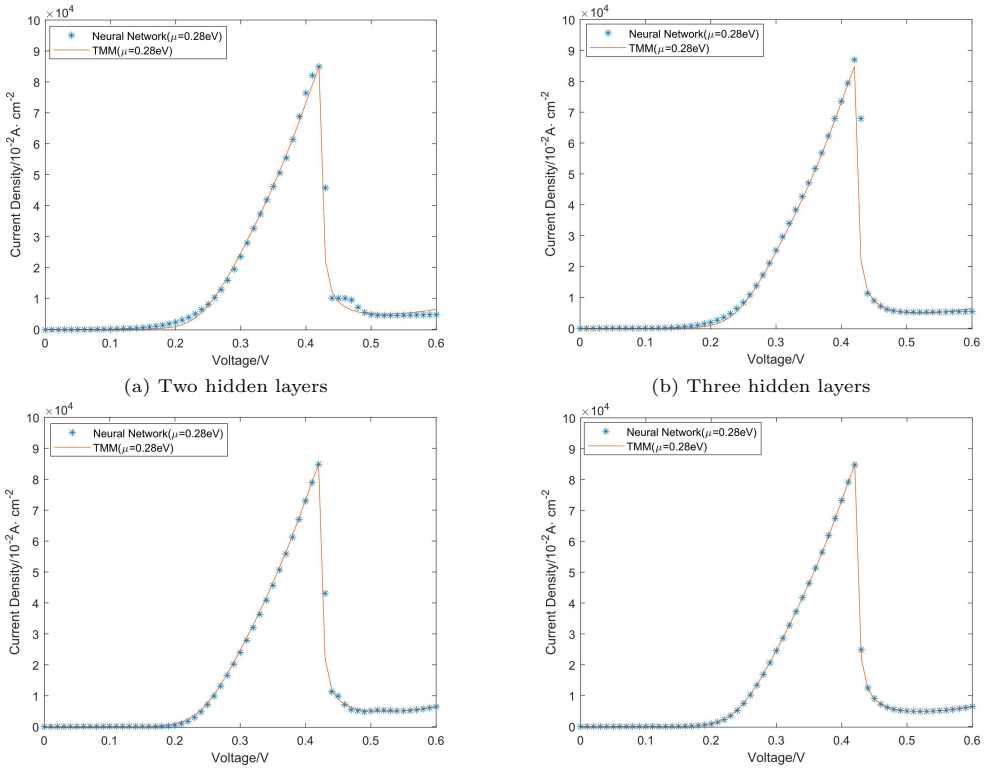

(a) Two hidden layers

(b) Three hidden layers

(c) Four hidden layers

(d) Five hidden layers

Fig. 4.9. Predicted the I-V curves using the fully connected neural networks.

5. Conclusion

In this research, we explored an efficient approach to achieve convergence in the I-V curves of the RTDs. The utilization of the TMM to solve the Schrödinger equation in the RTDs demonstrated superior convergence efficiency compared to alternative methods, both in the fixed potential scenarios and the self-consistent potential scenarios. Further simulations on a specific device, as discussed in Section 4.2, revealed that strategically increasing doping concentration throughout the entire device effectively mitigated tunneling bias and enhanced the peak current. Additionally, we employed shallow neural networks to fit the I-V curve using a limited dataset, resulting in networks with exceptional predictive capabilities.

Acknowledgments. This research was supported in part by the National Natural Science Foundation of China (Grant Nos. 12171035, 12371389, 12471378) and by the Natural Science Foundation of Guangdong Province of China (Grant No. 2024A1515010356).

References

[1] T.M. Abdolkader, H.H. Hassan, W. Fikry, and O.A. Omar, Solution of Schrödinger equation in double-gate MOSFETs using transfer matrix method, *Electron. Lett.*, **40**:20 (2004), 1307–1308.

[2] X. Antoine, A. Arnold, C. Besse, M. Ehrhardt, and A. Schädle, A review of transparent and artificial boundary conditions techniques for linear and nonlinear Schrödinger equations, *Commun. Comput. Phys.*, **4** (2008), 729–796.

[3] A. Arnold, Mathematical concepts of open quantum boundary conditions, *Transp. Theory Stat. Phys.*, **30**:4-6 (2001), 561–584.

[4] A. Arnold, M. Ehrhardt, M. Schulte, and I. Sofronov, Discrete transparent boundary conditions for the Schrödinger equation on circular domains, *Commun. Math. Sci.*, **10**:3 (2012), 889–916.

[5] A. Arnold, M. Ehrhardt, and I. Sofronov, Discrete transparent boundary conditions for the Schrödinger equation: Fast calculation, approximation, and stability, *Commun. Math. Sci.*, **1**:3 (2003), 501–556.

[6] R. Aronson and D.L. Yarmush, Transfer-matrix method for gamma-ray and neutron penetration, *J. Math. Phys.*, **7**:2 (1966), 221–237.

[7] H. Betsuyaku, Study of one-dimensional quantum spin systems by the transfer-matrix method, *Prog. Theor. Phys.*, **73**:2 (1985), 319–331.

[8] M. Cahay, M. Mclennan, S. Datta, and M.S. Lundstrom, Self-consistent I-V characteristics of ultra-small devices, *COMPEL - Int. J. Comput. Math. Electr. Electron. Eng.*, **6**:1 (1987), 53–57.

[9] S. Datta, Nanoscale device modeling: The Green's function method, *Superlattices Microstruct.*, **28**:4 (2000), 253–278.

[10] H.G. Deng, J. Guo, L.Q. Liu, and K.S. Zhou, An ameliorative arithmetic of Poisson equation for PN junction and its verification of Matlab, *J. Cent. South Univ. (Science and Technology)*, **39**:5 (2008), 913–917.

[11] W.L. Guo, Physical model of resonant tunneling diode: Lecture of resonant tunneling devices (3), *Micronanoelectron. Technol.*, **43** (2006), 167–171.

[12] X.F. He and K. Wang, Efficient approximation algorithm for the Schrödinger-Possion system, *Numer. Methods Partial Differential Equations*, **37**:1 (2021), 422–443.

[13] H.Y. Jiang, W. Cai, and R. Tsu, Accuracy of the Frensley inflow boundary condition for Wigner equations in simulating resonant tunneling diodes, *J. Comput. Phys.*, **230**:5 (2011), 2031–2044.

[14] H.Y. Jiang, T. Lu, and X. Yin, A hybrid explicit-implicit scheme for the time-dependent Wigner equation, *J. Comput. Math.*, **39**:1 (2021), 22–42.

[15] H.Y. Jiang, T. Lu, and W.T. Zhang, A hybrid sinc-Galerkin/finite-difference method for the time-dependent Wigner equation, *J. Comput. Appl. Math.*, **409** (2022), 114152.

[16] C. Jirauschek, Accuracy of transfer matrix approaches for solving the effective mass Schrödinger equation, *IEEE J. Quantum Electron.*, **45**:9 (2009), 1059–1067.

[17] B. Jonsson and S.T. Eng, Solving the Schrödinger equation in arbitrary quantum-well potential profiles using the transfer matrix method, *IEEE J. Quantum Electron.*, **26**:11 (1990), 2025–2035.

[18] A. Jüngel, *Transport Equations for Semiconductors*, Springer, 2009.

[19] R. Lake and S. Datta, Nonequilibrium Green-function method applied to double-barrier resonant-tunneling diodes, *Phys. Rev. B*, **45**:12 (1992), 6670.

[20] O. Pinaud, Transient simulations of a resonant tunneling diode, *J. Appl. Phys.*, **92**:4 (2002), 1987–1994.

[21] L. Sun, W.W. Yang, C.L. Xiang, Z.P. Yu, and L.L. Tian, A Broyden method for self-consistent solution of Schrödinger and Poisson equations, *Chinese J. Semicond.*, **26**:12 (2005), 2344–2349.

[22] X.Y. Wang, W.T. Guo, C.Z. Li, J. Lan, and W.Q. Sui, Introducing time-dependant sources for solving time-domain Schrödinger equation using FDTD method, in: *IEEE International Nanoelectronics Conference (INEC)*, IEEE, 2010, 746–747.

[23] T. Yokota and H. Betsuyaku, Study of one-dimensional Fermion model by the transfer-matrix method, *Prog. Theor. Phys.*, **75**:1 (1986), 46–58.

[24] P.J. Zhao, *Wigner-Poisson Simulation of Quantum Devices*, PhD Thesis, Stevens Institute of Technology, 2000.